Chapter 2

Near-Field Radar Microwave Imaging as an Add-on Modality to Mammography

Ashkan Ghanbarzadeh Dagheyan, Ali Molaei, Richard Obermeier, Aida K. Martinez and Jose Martinez Lorenzo

Additional information is available at the end of the chapter

http://dx.doi.org/10.5772/intechopen.69726

Abstract

According to global statistics, there is a high incidence of cancer in western countries; and, due to the limited resources available in most health care systems, it seems like one of the most feasible options to fight against cancer might be strict prevention policies—such as eliminating carcinogens in people's daily lives. Nevertheless, early cancer detection and effective treatment are still necessary, and understanding their efficacy and limitations are important issues that need to be addressed in order to ultimately enhance patients' survival rate. In the case of breast cancer, some of the problems faced by conventional mammography have been addressed in the literature; they include high rate of false-positive and false-negative results, as well as the possibility of overdiagnosis. New technologies, such as digital breast tomosynthesis (DBT), have been able to improve the sensitivity and specificity by using 3D imaging. However, the low contrast (1%) existing between tumors and healthy fibroglandular tissue at X-ray frequencies has been identified as one of the main causes of misdiagnosis in both conventional 2D mammography and DBT. Near-field radar imaging (NRI) provides a unique opportunity to overcome this problem, since the contrast existing between the aforementioned tissues is intrinsically higher (10%) at microwave frequencies. Moreover, the low resolution and highly complex scattering patterns of microwave systems can be enhanced by using prior information from other modalities, such as the DBT. Therefore, a multimodal DBT/NRI imaging system is proposed to exploit their individual strengths while minimizing their weaknesses. In this work, the foundation of this idea is reviewed, and a preliminary design and experimental validation of the NRI system, used as a DBT complement, is introduced.

Keywords: breast cancer detection, microwave imaging, near-field radar imaging, antipodal Vivaldi antennas, digital breast tomosynthesis, breast cancer statistics

1. Introduction

According to the most recent statistics from SEER [1], around 14, 140, 254 individuals were living with a type of cancer in 2013; and, based on the 2011–2013 data, approximately 39% of men and women will be diagnosed with cancer during their lifetime in the US [1]. Particularly, breast cancer is the most prevalent cancer in terms of incidence, and it is the second cause of cancer death among women after bronchus cancer [2]. Furthermore, the data from 1975 to 2013 illustrates that the incidence of breast cancer has had either an ascending or irregular trend across almost all races in the US. Mostly due to advancements in detection and treatment, the rate of mortality has decreased. However, looking at the incidence statistics, it is clear that the efforts in preventing breast cancer can still be improved [1, 3]. Environmental factors such as exposure to ionizing radiation, inheriting certain genes such as BRCA1 and BRCA2, and, most importantly, lifestyle have been associated with an increase in the risk of breast cancer. For instance, the link between breast carcinogenesis and naturally occurring substances such as heterocyclic amines (HCAs), insulin-like growth hormone (IGF-I), animal estrogen (E2), and bovine leukaemia virus (BLV), which are ubiquitous in western and modern diets, have been substantiated with a vast body of evidence [4–11]. Nonetheless, not much has been done in updating the dietary guidelines and food policies to address the role of these substances, and similar ones, in cancer epidemic. In parallel, statistics show that, in general, the rate of breast cancer and other types of cancer are appreciably higher in western and industrialized countries [12], which can be attributed to both advanced detection technologies and lifestyle. The experience from Japan's transition towards adopting a western diet and the dramatic increase in cancer and Alzheimer's disease rates [13–15] as well as Japanese-American immigrants' higher risk of cancer compared to the people residing in Japan [16], are in accordance with the mentioned statistics. Similar observations have been made in the case of ischemic heart diseases [16, 17] and Alzheimer's disease [18] in other countries. These studies report that (1) in some countries such as Uganda coronary heart diseases only happened in rare cases, in contrast to the global trend in which ischemic heart disease is the number one cause of death; and (2) despite the high frequency of Alzheimer's genes (APO E 4 allele) in countries such as Nigeria, the disease itself is not as nearly prevalent as in western countries. **Figure 1** recapitulates the aforementioned statistics of breast cancer. Until interventions are made to eliminate the possible causes of breast cancer–and cancer in overall–and to seriously implement prevention programs, early detection via imaging and other screening tools and advanced treatment techniques are probably the only temporary solutions to address this matter.

One of the new early detection methods for breast cancer that has attracted much attention during the last decade is near-field radar imaging (NRI) with microwaves. Though microwave imaging is limited by low resolution, it can provide additional information about the breast composition, since the contrast between malignant and healthy fibroglandular tissues at microwave frequencies is more than that at X-ray frequencies. This chapter is aimed at describing a microwave imaging system that can be added to digital breast tomosynthesis (DBT), also a novel 3D X-ray machine, to make possible a bimodal screening method. Firstly, the shortcomings of mammography as the most widely used screening method is briefly reviewed to show the necessity of introducing novel and more accurate breast imaging methods. Then, the

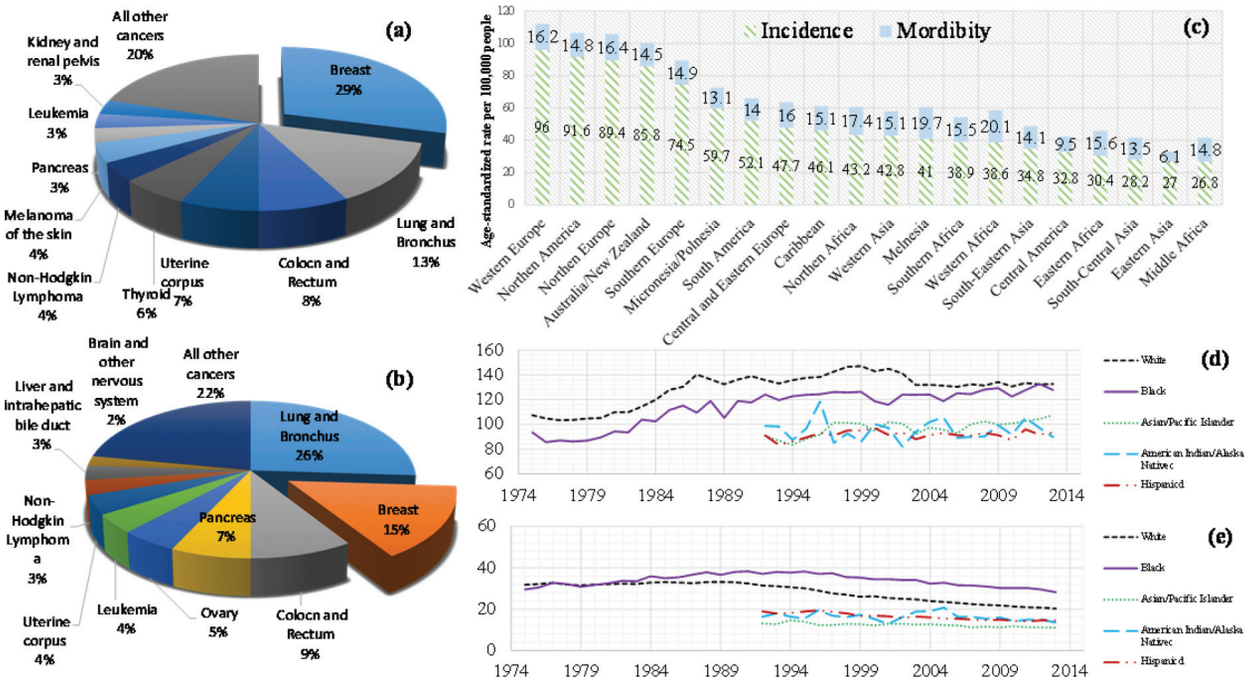

Figure 1. Breast cancer statistics in the US and the globe at glance: (a) Incidence and (b) mortality rate with respect to other types of cancer in the US, (c) incidence and mortality rate compared among a number of countries, (d) incidence and (e) mortality rates in the US from 1975 to 2013.

possible benefits and details of adding a near-field imaging system to X-ray mammography is discussed. It is predicted that the final bimodal, NIR-X-ray (DBT), imaging system has the potential to improve true-positive (TP) diagnosis.

2. Drawbacks of mammography

Mammography, as the most widely used modality for population-based breast cancer screening, employs X-ray radiation to reconstruct images of the breast. Inspite of the 34% reduction in breast cancer morbidity rate [19] attributed mainly to advancements in detection and treatment, more research is yet needed to find more effective imaging and treatment methods. Despite the contributions of mammography to this reduction, the possibility of false-positive results, false-negative results, and overdiagnosis associated with it, as addressed in the literature, has raised some substantiated concerns. These three inherent shortcomings of current X-ray imaging technology are briefly reviewed in the following subsections.

2.1. False-positive results

A false-positive (FP) outcome is referred to a case where the breast is actually cancer-free, but the mammogram is misread as abnormal. In the New England study in 2000, the risk of obtaining an FP result was estimated to be 6.5%, and it was reported that at least 23.8% of the study participants received an FP result [20]. The risk could go up as high as 43.1% after nine mammograms. Another study reported a prevalence of 10.6% of FP results among women in

the age range of 50–51 in their first mammography session. In the following sessions, the probability was approximated to be 3.8%; but the cumulative risk of getting an FP outcome turned out to be 32.4%, implying that one out of three women could receive an FP alarm during a 10-year biannual screening program [21]. The large study performed in 2011 reported that there is a prevalence of 16.3 and 9.6% in obtaining an FP result in the first and following sessions, severally. The cumulative risk was found to be 61.3% for women starting their regular session at the age of 40 or 50, in an annual screening program [22]. Before the possibility of breast cancer is ruled out, a patient who receives a positive result is recalled for further examination that usually includes ultrasound imaging, needle biopsy, and sometimes surgical biopsies. These biopsies, which some authors call "unnecessary" [23, 24], as well as the prolonged uncertainty about ones' health status, can be accompanied by a psychological trauma similar to those who were diagnosed with cancer in their first 6 months with symptoms such as short-term anxiety, more frequent self-examinations, and a change in the patients' tendency to attend later mammography sessions [25–28]. It has also been reported that 27 and 33% of women gone under breast biopsy had reduced sexual sensitivity and pain in the breast. In addition, an increment in mood disturbances and reduction in natural killer cell activity and INF γ production was observed before and after biopsy [26, 27]. Therefore, FP results can lead to serious consequences that need to be addressed.

2.2. False-negative results

As the name implies, when a malignant tissue is not detected in a mammogram, the result is a false-negative (FN). The tumor might be detected in the next screening sessions, when perhaps it has grown visible due to invasion into the encompassing tissues. The data on the prevalence of FN results has been inconsistent. In a 1996 study, it was found that, depending on family history, follow-up duration, and age; between 12.5 and 31.5% of mammograms were interpreted as cancer-free, while there was actually a tumor in the breast [29]. A more recent study, in 2014, showed that FN probability in digital and screen-film mammography for women above (under) 50 was 24% (27%) and 27% (24%), respectively [30]. It was reported that obtaining an FN result was directly associated with breast density. Other factors that play a role in FN evaluation of breast are the type of cancer (particularly BRCA 1 and BRCA 2 mutations) and the location of the tumor (being close to the chest wall) [31, 32].

2.3. Overdiagnosis

Overdiagnosis may be defined as "the detection of cases that would never have come to clinical attention without screening [in a patient's lifetime] [32]." Though some physicians disagree with the numbers reported for such cases [33]. Some studies from 2004 reported overdiagnosis rates of 5% in ductile carcinoma *in situ* (DCIS) in Italy [33] and 33% in general mammography of women of ages 50–59 in Norway and Sweden [34]. The results from the later study were comparable with the 30% rate of overdiagnosis reported in [35], back in 2001. A larger study in 2005, which was carried out over eleven counties in Sweden, reported the risk of overdiagnosis as 21 and 54% for women in age groups of 50–59 and 60–69, in order [37]. The prevalence of subclinical tumors among women after 50 was explained as the reason for rather high risks of overdiagnosis. On the other hand, a recent report in 2015 from South

Australia reported the overdiagnosis risk as 8% for invasive cancer and 12% for when cases of DCIS were included in the data [36]. Also, a review on studies conducted in European countries reported the risk to be 1–10% [37]. The discrepancies in numbers reported by different researchers is illustrative of the complexities involved in estimating breast cancer overdiagnosis.

Based on the problems described in this section, the necessity of investigating new science and developing novel technologies for breast imaging, either as complementary or standalone modalities, is evident. The focus of the work presented in this chapter is on reducing false-positive and false-negative results by fusing the information acquired by two different modalities. However, overdiagnosis cannot be addressed with the current status of the add-on NRI unit.

3. Digital breast tomosynthesis (DBT)

About 40% of eligible women who are recommended to have regular screening have dense breasts, which are composed of more than 50% glandular tissue and are among the major contributors to uncertain mammogram readings [38, 39]. Thereby, one of the focuses of new screening devices is to enable better imaging visibility through different layers of breast. This is not properly addressed in conventional 2D mammograms of the breast; since an existing tumor can be masked by underlying and overlying tissues and, thus, make accurate diagnosis difficult for radiologists. In order to enhance the image resolution, full-field digital mammography (FFDM) detectors can be utilized. The DBT employs these detectors as well as a rotating X-ray tube that moves in a circular arc to illuminate the breast from different angles [40]. Then, images of several 2D projections at dissimilar depths are reconstructed, making it feasible for radiologists to look through different layers. Aside from hardware enhancements, novel imaging algorithms –including, but not limited to, filtered back projection and Gaussian frequency blending; and iterative techniques such as Maximum Likelihood and Simultaneous Algebraic Reconstruction Technique—have been applied in the DBT on the software level [40].

Conventional mammography makes use of film-screening, which provides high resolution to delineate micro-calcifications and other fine features in the breast; yet, it has a narrow dynamic range that limits tumor visualization in dense segments of the breast. FFDM, however, improves dynamic range and provides the radiologists with the option to manipulate the reconstructed images. Moreover, higher contrast is observed between dense glandular and fatty tissue when FFDM detectors are used [40]. The efficacy of the DBT has been put to the test to evaluate how effective its new features are in practice. In a study in 2005, it was reported that for the age group under 50, premenopausal women, and patients with consistently or extremely dense breasts; the accuracy of images acquired by digital mammography was higher than that of conventional mammography [41]. Additionally, it was shown that the margin, calcification, and lesion visibility of the DBT was superior to conventional imaging in the images of an FDA-certified breast phantom. The radiation exposure levels were similar or less in the DBT; and the tumor boundaries and vessels around calcifications were clearer, which contribute to better identification of malignant and benign masses [42]. Based on the

better lesion visibility of the DBT, Teersa et al. recommended tomosynthesis as a complementary modality to 2D mammography [42]. The combination of 3D and 2D mammography is more commonly adopted than 3D imaging alone in clinical settings [40].

The improved accuracy using 2D-3D mammography was also observed by Bernardi et al. [43, 44]. Better visualization of tumors, as provided by a 2D-3D setup could reduce the number of FP results and consequently result in fewer follow-up biopsies. Consistent with this prediction, in 2009, Gur and others reported 10% decrease in false-positives when DBT was used in addition to FFDM [45]. In a more recent study in 2014, the ascendency of 2D-3D mammography over 2D mammography was substantiated in terms of true-positive evaluation and sensitivity [46]. In the same year, Bernardi's subsequent study showed a considerable elevation, from 60% in 2D to 87% in true-positive readings of radiologists when using a 2D-3D configuration [47]. One year later, Svahns et al. considered the FP to TP ratios in three population-based studies and reported improvements in radiologists' interpretive efficacy of X-ray images when a combined configuration was implemented. The results indicated 55, 48 and 30% improvement in true positive detection when a 2D-3D setup was used in lieu of traditional setup in Houston, STORM, and Oslo studies, severally [48]. In TOMMY trial in UK, 2015, increased specificity (by 9%) for all studied groups and elevated sensitivity (by 7%) for dense breasts was observed as a result of using digital and film screening [49]. A 2016 review also reported fewer recall rates using the DBT [50].

4. Breast near-field radar imaging (NRI)

4.1. Background

The contrast between cancerous and fibroglandular tissues is higher when they are exposed to microwave radiation than when they are illuminated by X-ray [53]. This contrast is increased about 5–10 fold when moving form X-ray to microwave frequencies, contingent upon the operating frequency span [51, 52], which renders microwave imaging a distinct candidate to be used as a complementary modality to 2D-3D mammography. A large study by Lazebnik et al. showed that the difference between dielectric properties of malignant and normal tissue is 10% when the fibroglandular tissue is in the background and 10:1 when the adipose-dominant tissue is considered as reference [53]. Though the former is significantly lower than the adipose/tumor contrast, it is still remarkably higher than the fibroglandular/tumor contrast in X-ray frequencies, which is about 1% [54]. **Figure 2** displays the *ex vivo* tissue properties as reported in [53] and as can be observed, the dissimilarity between the fibroglandular and malignant tissue is appreciable. Halter et al. showed that the difference between the dielectric properties of healthy and malignant tissues measured *in vivo*, using microwave and electrical impedance spectroscopy during reduction surgeries, is decreased [54]. However, the contrast is still adequately large for NRI to be a technique of interest as an improvement to conventional or digital mammography. Meaney et al. also pointed out that even though the *in vivo* measurements exhibit lower microwave contrast of about 2:1 (tumor permittivity: average permittivity of breast) at 0.9 GHz, the difference is still significant compared to that in most other traditional imaging systems [52]. Besides high complex permittivity values, there are other features that

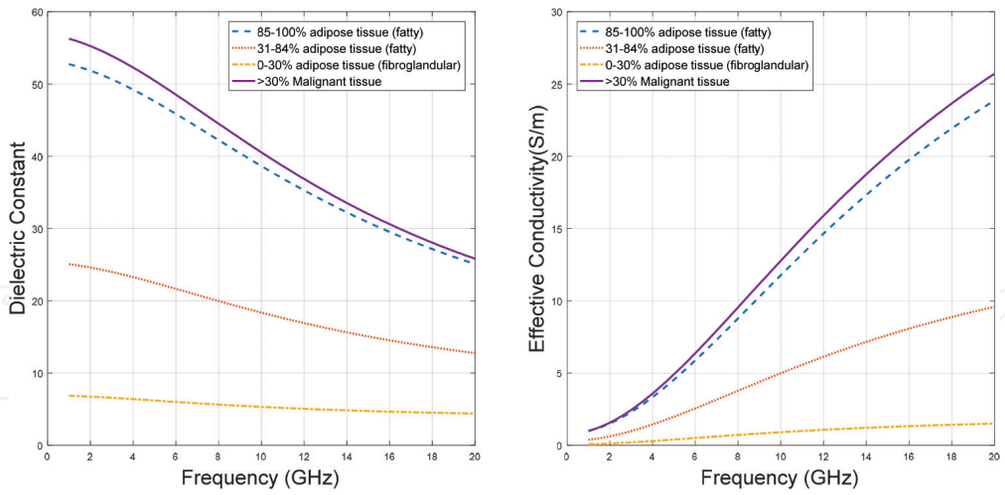

Figure 2. Comparison between the dielectric properties and conductivity of healthy tissues and malignant tissues. Plots are based on the data from [53].

make NRI a suitable candidate for breast screening. It is intrinsically non-ionizing and it does not require breast compression when used independently. Also, microwave imaging provides high sensitivity for revealing small-sized masses. These qualities come at a considerably lower cost than other methods such as nuclear medicine and magnetic resonance imaging (MRI) [55].

To be able to reconstruct images of breast in microwave frequencies, several studies have been dedicated to find practical imaging algorithms including [56–58] that introduce finite difference time-domain (FDTD) and finite element techniques. Among other introduced methods, iterative numerical techniques such as conjugate gradient least square, Newton-Kantorovish, and Levenberg-Marquardt [59–61]; as well as finite difference frequency-domain (FDFD) can be mentioned [62–67]. The moderate imaging resolution in current clinical layouts can be enhanced via novel algorithms such as solving the 3D inverse problem employing variable-strength spatial prior constraints [66] and applying compressive sensing confocal imaging algorithms [67]. Both of these methods present encouraging results for the future of NRI. Making use of prior geometry or information, acquired by other imaging modalities, for microwave imaging is an ongoing research subject that can facilitate breast tomography and image reconstruction. Two recent works in this area used microwave radar imaging and MRI to feed the dielectric parameter reconstruction codes with spatial information. Baran et al. restored the average dielectric properties of different tissue types by microwave radar imaging and then used the data to perform microwave tomography [68]. They were able to obtain finer reconstruction qualities using this hybrid method than when tomography and radar-based imaging were conducted separately. Golnabi et al. employed an MRI image to reconstruct the complex permittivity of a real breast [69]. They reported improved accuracy and contrast between the target and background medium that were fibroglandular and adipose tissues, respectively. One year later, in 2016, they implemented this idea in a 3D reconstruction and again achieved promising outcomes with up to 2 and 9 times improvement in accuracy of conductivity and permittivity maps, respectively [70]. Due to the interference of metallic parts with the magnetic fields, combining microwave imaging and MRI in the same physical setup was reported to be unfeasible.

4.2. Breast NRI at experimental level

One of the first NRI system implementable for a clinical trial was introduced in 2000 by Meaney and his colleagues [52]. The operational bandwidth of the system was 0.3–1 GHz and it was configured in a way that a patient could comfortably lie down on a bed with her breast pendent in a liquid inside a container with a circular antenna array encompassing the breast. The antennas were immersed in the same liquid (saline) as the matching medium, and they collected the scattered field from the submerged breast from multiple directions. The scan took 10–15 min for each breast of the human participants of the trial, using a tomographic method from the chest to the nipple. As predicted, the reconstructed maps of dielectric properties were of low resolution; however, they showed that the *in vivo* breast properties are larger than the ones obtained from *ex vivo* measurements. Later in 2007, the same group reported a good agreement between images retrieved by microwave imaging and MRI from subjects with normal mammograms and multiple phantoms [66]. Particularly, it was shown that fibroglandular tissue distribution and water content agreed well between the two sets of images. Furthermore, they found that similar to fat percentage and density, dielectric properties of the breast are heterogeneous.

Klemm et al. assembled a similar physical setup except, in place of a circular antenna, they used a set of ultra-wideband (UWB) antennas that were arranged in a hemispherical shape to conform to the shape of the pendent breast [71]. The system's performance was evaluated based on experiments carried out on a phantom encapsulated in a shell mimicking skin. They were able to detect small tumor simulants, 4-6 mm in diameter, embedded in the phantoms by implementing two beamforming algorithms, multi-static microwave imaging (MAMI) and delay-and-sum (DAS). Later, the system was tested on highly heterogeneous phantoms and it was shown to give promising results [72]. Also, in a clinical case study, the system was tested on a real breast, and the obtained image was compared to its associated mammogram. The malignant tissue was correctly located in the microwave image when compared to the X-ray image [73].

Lai and his group also employed UWB antennas to scan a number of heterogeneous and homogenous breast phantoms at Nanyan Technological University [74]. By rotating the phantoms 360 degrees, the antennas simulated a circular set of 360 elements. This configuration enabled them to detect a 4 mm tumor in all phantom types. But, detectability was not strong enough to delineate 2 mm inclusions. Lazero et al. published the results of what they named a "worst-case-study" utilizing a single UWB monopole antenna [75]. The phantom model was filled with water (presenting high losses), with a rod submerged inside it, and the antenna was located in air (presenting high reflection). Notwithstanding these challenging conditions, the embedded rod was successfully detected, implementing FDFD and Wiener-filter algorithm that took into account the effect of a simulated skin interface. Chun Yu and colleagues, in a different experimental layout, used an active microwave imaging method to retrieve images of a clay ball, a metallic ball, and a combined arrangement of both when they were submerged in water [76]. They utilized a dipole single transmitter and receiver to avert the mutual coupling that exists in an antenna array. The transmitting and receiving array were moved by an automatic positioner to enable a flexible, multi-view data acquisition in three dimensions over the surface of the object being measured. Applying an active, hybrid-inversion, reconstruction method, they were able to image one clay ball and the combined arrangement of two clay balls and one metallic ball.

Henriksson et al. made use of a microwave camera, at 2.45 GHz, to quantitatively restore the dielectric properties of materials [77]. In a quantitative approach, in place of approximations, the non-linear diffraction problem is solved at the cost of heavy computations. In 1990, the planar camera was built for non-invasive hyperthermia control; and later, in 1998, it was put to the test by Franchois on a rotating object inside a liquid container. Henriksson and his colleagues used a similar experimental setup that included two horn antennas. They made a breast-equivalent liquid using a Triton X-100 mixture and placed it inside a rotating tube—the object of interest—to have a more realistic model. Albeit some artifacts were present, the system performed well in reconstructing dielectric maps, using the Newton-Kantorovich algorithm. This camera enables NRI to be carried out in a mammographic configuration [77, 78], one of the key benefits of the approach presented in this chapter. More recently, in 2013, imaging a moving target was also tested in an integrated microwave imaging radar, as in an inverse synthetic array radar, at the University of Padova in Italy [79]. In the assembled setup, a planar antenna, consisting of two monopoles and two feed lines, was fixed on a support frame and it radiated down over the moving phantom. Two stepper motors shifted the target in the horizontal plane in two perpendicular directions. The results demonstrated that the system is capable of detecting two embedded inclusions inside the phantom.

Microwave imaging via space-time (MIST) beamforming has been experimentally implemented on phantoms, seeking to solve both 2D and 3D problem. On the simulation level, Bond et al. used a UWB antenna array to transmit the waves and then employed a beam former to reconstruct images of the backscattered signal energy [80]. In order to downsize the overshadowing impact of the skin-like layer of the MRI breast model they used, they utilized a data-adaptive algorithm to eliminate the dominant backscatter at the skin-breast interface. This approach is efficient in that it generates images only in areas of high background energy, i.e. malignant tissues. In the subsequent year, from the same group, Xi Lu et al. tested the practicality of MIST on 3D physical phantoms [81]. The results in 2D and 3D improved considerably compared to those obtained by simple focusing methods. In the 3D case, the contrast between malignant and normal tissue was observed to be 1.5:1 for a 4-mm tumor, which displayed the strong potential of MIST in disclosing small tumors.

At the end of this subsection, some of the recent works that are different in application or scope from the ones previously introduced can be reviewed to show how the practical aspect of microwave imaging has expanded in last few years. In 2014, Eleutério et al. presented a preliminary study to evaluate NRI in the axilla where sentinel nodes are typically found [82]. The significance of this study was to explore the role of microwave imaging in the estimation of metastasis initiation. Grzegorczyk et al. applied microwave imaging to monitor neoadjuvant chemotherapy, as an economic alternative to MRI and PET [83]. Using a different and compact method, researchers at the University of Manitoba examined the capacity of spintronic microwave sensors in biomedical imaging [84]. They demonstrated that these sensors, though only a fraction of microwave antennas in size, have the ability to detect spherical objects inside a homogenous medium with good resolution. Contrast-enhanced NRI has also become a topic of interest in the recent years. In one of the latest works published in 2016, Bucci et al. used magnetic nanoparticles as contrast agent, and showed their applicability by comparing the simulation and laboratory results [85].

5. A near-field radar imaging system for bimodal applications

In the last two sections, some aspects of mammography, digital tomosynthesis, and microwave imaging were reviewed. The idea of a bimodal system that takes advantage of the strengths of both systems and can potentially compensate some of the drawbacks of each modality makes sense in the case of NRI and DBT. Among the number of other different combinations that has been tested in the last few years, NRI and MRI, optical imaging and DBT, and NRI and ultrasound can be listed. In the first case, the interference of the magnetic fields with the metallic part of the microwave imaging system impeded the simultaneous implementation of the NRI and MRI sensors [86], but in the other two cases, important results such as access to the map of vessels around tumors via the optical modality [87] and detection of very small inclusion [88], down to 1.2 mm, were reported. One of the pragmatic ways by which NRI can be added as a complementary system to the DBT is to design and build a compact NRI system that conforms to the geometry of the DBT and can scan the breast in a co-registered fashion using mechanical motion. This idea is illustrated schematically in **Figure 3**: (1) to conform to the DBT's shape, the NRI system was designed to fit into the compression paddle, (2) to be as compact as possible, a set of antipodal Vivaldi antennas (AVAs) were used as the transducer array, (3) to enable mechanical motion, a two-dimensional motion stage was implemented. In the succeeding subsections, the various parts of the system are described in more details.

5.1. Antipodal Vivaldi antennas (AVAs)

Vivaldi antennas are planar, compact in size, and easy to manufacture [91]. These qualities make Vivaldi antenna a good candidate for use in an add-on NRI system, particularly due to

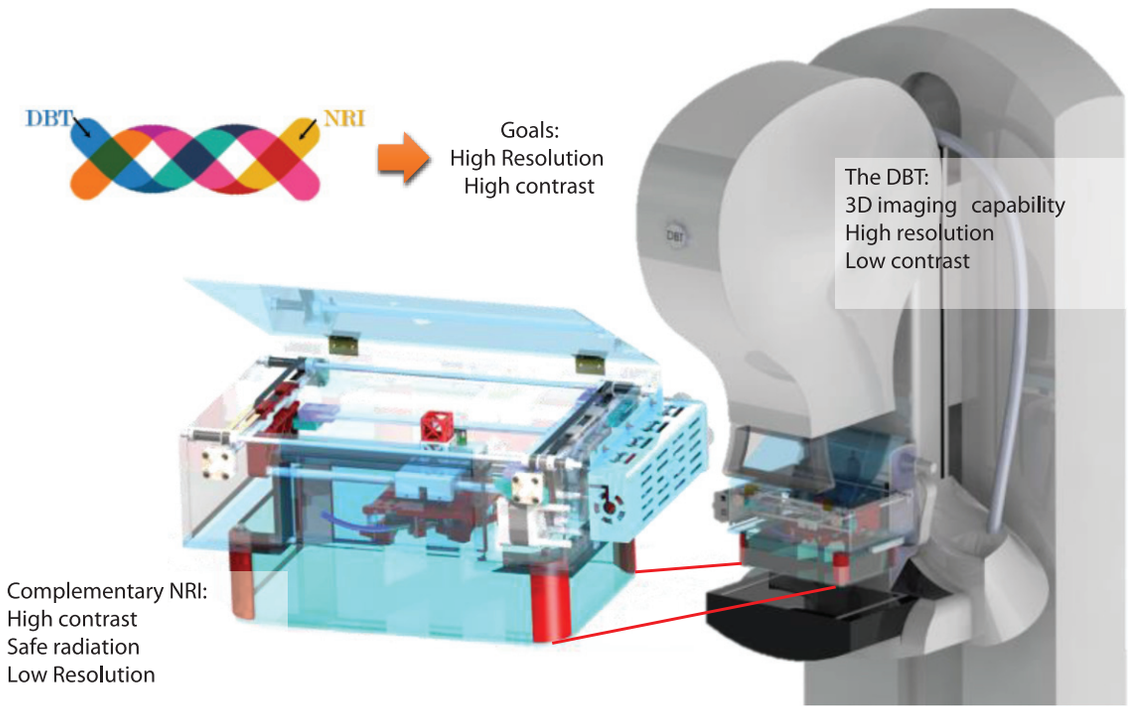

Figure 3. The designed NRI mechatronic system (left) that fits into the compression paddle of the DBT (right). In this manner, first the DBT and then the NRI system scans the breast.

that a number of these antennas can fit into a small space [89]. On the other hand, Vivaldi antennas are limited in bandwidth since they require a balun to convert the micro-strip into a strip-line. One solution to remove this obstacle is to employ antipodal vivaldi antenna (AVAs) that have direct feeding micro-strip lines while maintaining the advantages of Vivaldi antennas. To further reduce the size of the AVAs and improve the coupling of electromagnetic waves going into the breast tissue, they can be designed to operate in a liquid of high dielectric constant. The use of a matching liquid can cut each dimension of the antenna by a factor of $1/\sqrt{\varepsilon_r}$, with ε_r being the liquid relative permittivity. Such a technique, however, asks for a supportive substrate that also has a high dielectric constant. This imposes an extra condition on the selection of the coupling liquid that will be discussed later. In the case of AVAs of the proposed system, a 2 mm ceramic layer (T-Ceram, E-37) with a relative permittivity of 37 was utilized for each antenna. **Figure 4** shows the design parameters of an AVA alongside with a photo of a pair of fabricated AVAs. The exponential curves y_a, y_t, and y_f shown in the figure are given by the following Eq. [90]:

$$y_k = \pm\left(A_k e^{P_k(x-B_k)} + C_k\right) \tag{1}$$

where

$$A_k = \frac{y_{k1} - y_{k2}}{e^{P_k(x_{k1}-B_k)} - e^{P_k(x_{k2}-B_k)}},\ C_k = \frac{y_{k1}e^{P_i x_{k2}} - y_{k2}e^{P_k x_{k1}}}{e^{P_k x_{k2}} - e^{P_k x_{k1}}} \tag{2}$$

and k can be substituted with a, t, or f to obtain y_a, y_t, or y_f, in order. The subscripts 1 and 2 for x denote the x-coordinate of the start point and endpoint of the curves. The constants A_i, B_i, C_i, and P_i for every equation are given in **Table 1**. The numerical values of the parameters for the

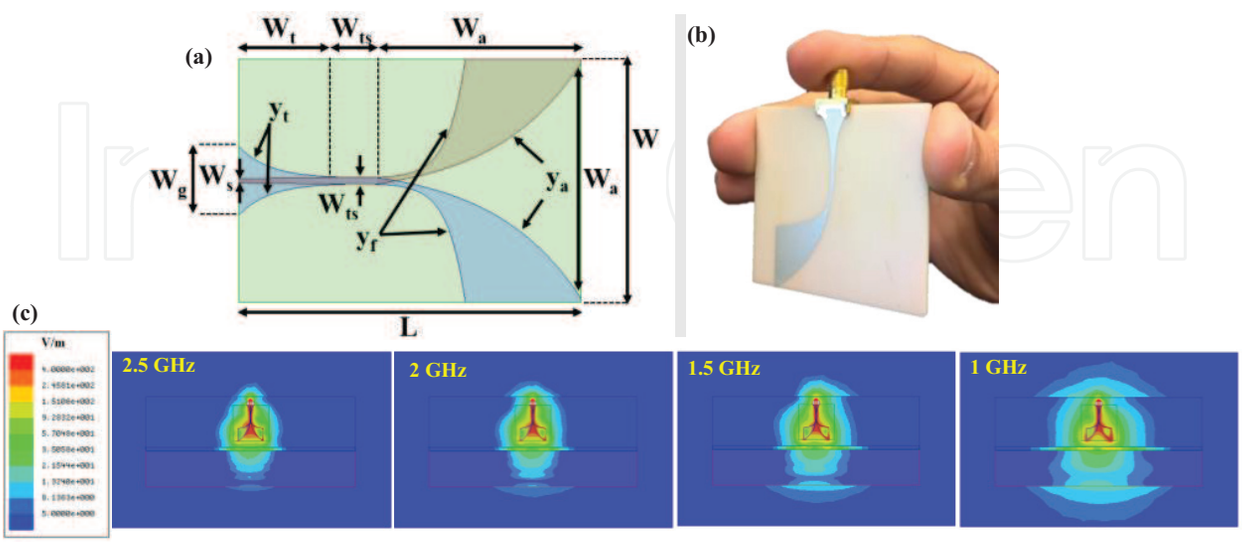

Figure 4. (a) Design parameters of the AVA used in the system. This transparent view of the antenna shows the curves on front (signal) and back (ground) of the antenna. (b) The fabricated antenna has a reduced size, as it can be seen when the size is compared to a person's hand. (c) The simulated results showing the magnitude of the electric field inside an ethanol model at different frequencies.

$y_i(x)$	A	B	C	P
y_t	$\frac{W_{ts}-W_g}{2(e^{P_t L_t}-1)}$	0	$\frac{W_g}{2}-A_t$	P_t
y_f	A_f	W_t+W_{ts}	$\frac{W_{ts}}{2}-A_f$	P_f
y_a	$\frac{W_{ts}+W_a}{2(e^{P_a L_a}-1)}$	W_t+W_{ts}	$-\frac{W_{ts}}{2}-A_f$	P_a

Table 1. The definitions of the parameters A, B, C, and P in the curve equations of the AVA.

fabricated antennas were $W = 30$, $W_g = 2.06$, $W_a = 25.42$, $W_{ts} = 0.29$, $W_s = 0.025$, $L_t = 8.40$, $L_{ts} = 1.03$, $L_a = 26.54$, all in millimetres, and $P_t = -1.04$, $P_f = 0.94$, $P_a = 0.1$ [91]. The radiation pattern of a single antenna is illustrated in **Figure 4 (c)** at different frequencies.

To select the coupling liquid, the dielectric relaxation of many liquids, such as [92–102], were considered. John D. et al. used multi-step techniques to approximate the average dielectric properties of the breast tissue and reported a minimum and maximum of about 26.5 and 27 for the relative permittivity in 1–3 GHz, respectively [103]. For a proper coupling of the electromagnetic waves, the average dielectric constant of the sought liquid must be between the relative permittivity of the antenna substrate (37) and that of the average breast (26.75). Based on this criterion and other conditions such as non-toxicity, non-carcinogenicity, low viscosity, and stability at room temperature, among many candidates, ethanol was selected as the matching liquid. The characterization of an array of two AVAs in ethanol can be found in [104].

5.2. Radiation safety: Specific absorption rate (SAR)

To assure that the microwave radiation from the antennas was safe for human use, a specific absorption rate (SAR) analysis was conducted. The SAR determines the amount of power absorbed by the human tissue when it is exposed to the electromagnetic radiation [105]. The local SAR at a certain point inside the tissue is defined as

$$SAR_{local}(\boldsymbol{r}, \omega) = \frac{\sigma(\boldsymbol{r}, \omega)|E(\boldsymbol{r}, \omega)|^2}{2\rho(\boldsymbol{r})} \tag{3}$$

where $\boldsymbol{r}$ is the position vector, ω is the frequency in $[rad/s]$, $\sigma(\boldsymbol{r}, \omega)$ is the material conductivity in $[S/m]$, and $\rho(\boldsymbol{r})$ is the mass density of the dielectric. For standardization purposes, SAR is averaged over a small sample volume as follows:

$$SAR_{average}(\boldsymbol{r}, \omega) = \frac{1}{V}\int \frac{\sigma(\boldsymbol{r}, \omega)|E(\boldsymbol{r}, \omega)|^2}{\rho(\boldsymbol{r})} d\boldsymbol{r} \tag{4}$$

This power flow reveals itself in the form of temperature gradient over time, and it could cause harm if it trespasses a certain value. Federal Communications Commission (FCC) in the United States has set a threshold of 1.6 W/kg for the maximum value of SAR in a 1-gram sample of body parts [105]. In Europe, as set by The Council of the European Union (CEU), the limit is 2 W/kg in a 10-gram sample of body parts [107]. IEEE Standard 1528 presents a methodology to compute the peak SAR in the head under exposure to radio frequency radiation [108, 109].

This can also be applied in other body part calculations. HFSS ANSYS, which automatically applies IEEE standard P1528.4 to calculate the spatial average of SAR [111], was utilized to analyze the SAR of the heat that an AVA induces in a breast model placed directly underneath it. The model consisted of fat distribution data from a real healthy breast, obtained by the DBT system at the Massachusetts General Hospital (MGH). **Figure 5 (a)–(c)** illustrates the fat distribution in the model from different views. In lieu of importing the entire data set into the HFSS, the fat percentage values were averaged over cubes of 6 mm side to lessen the computational load. Next, the complex relative permittivity of the breast was approximated by a Cole-to-Cole model. The impact of the breast compression paddle and the ethanol container were also accounted for by using a simplified geometry of the NRI system, as shown in **Figure 5 (d)–(e)**. In accordance with the real measurements, the power fed to the antennas

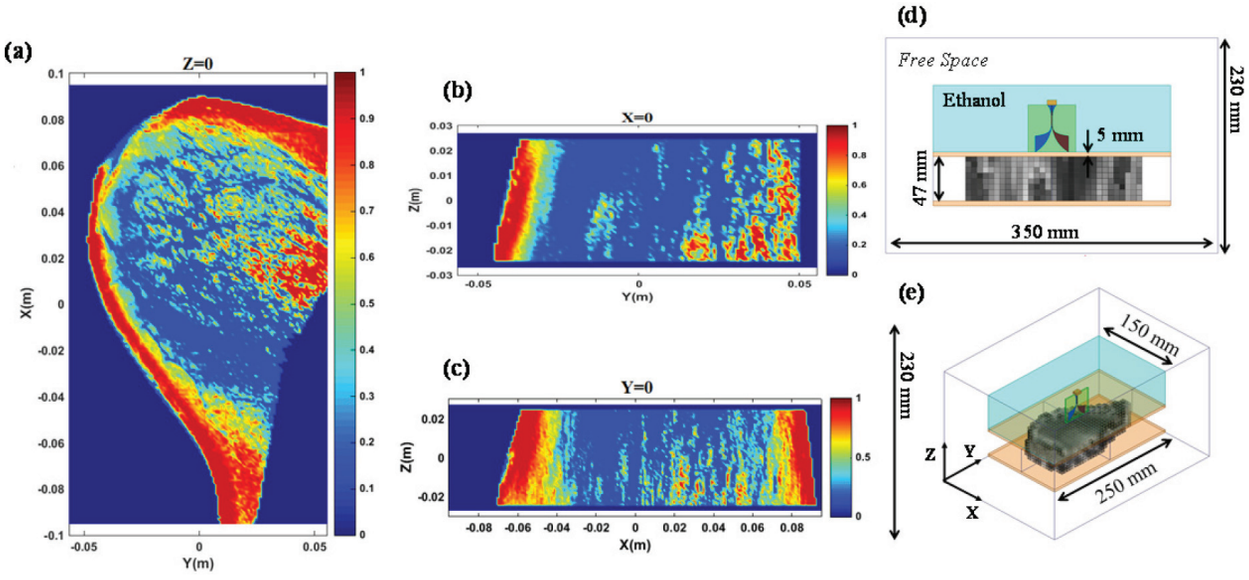

Figure 5. The fat distribution map of a real healthy breast used to compute the complex dielectric constant [106], and its associated model. The map as viewed from (a) top, (b) side, (c) front. The approximated model in a voxel grid of cubes of 6-mm sides, from (d) front and (e) perspective view.

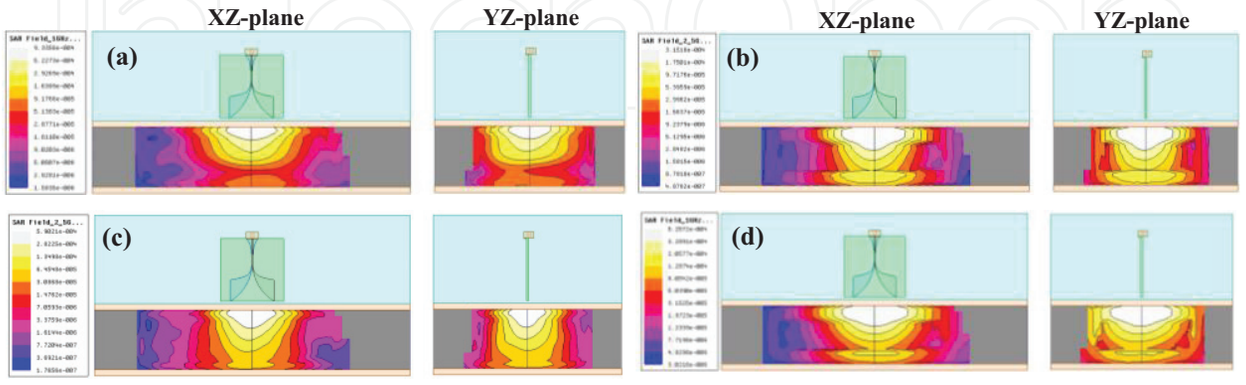

Figure 6. The SAR study results of one antenna radiating towards the breast model: (a) 1-gram sample at 1 GHz, (b) 10-gram sample at 1 GHz, (c) 1-gram sample at 2.5 GHz, (d) 10-gram sample at 2.5 GHz. The maximum value of the SAR occurs at 1 GHz in the 1-gram sample model and is much less than the threshold value set by the FCC.

was set to 0 dBm (1 mW). The results for both 1- and 10-gram sample SAR models at two dissimilar frequencies in the operational bandwidth of the system, 1–3 GHz, are shown in **Figure 6**. As observed, the peak SAR values are clearly below the CEU and FCC thresholds, by at least three orders of magnitude, in all cases. This suggests that the radiation from the transducer array, even with an array of sixteen antennas, is safe for human use.

6. The mechatronic system: Motion stage and data acquisition

6.1. The hardware

As mentioned earlier, to illuminate the entire breast volume under compression, the antennas needed to be moved in a pre-determined trajectory. To accomplish this, a belt-driven mechanical setup was implemented based on the open-source 3D printer, MAKERBOT Replicator. Two motors were used, one for each axis of motion, to enable the planar motion. One of the motors (Y-axis) was fixed to the walls of the container, and the other one (X-axis) was mounted on a carriage that itself moved as the first motor shaft rotated. The dimensions and other geometric properties of the box containing all the mechanical parts were majorly restrained by the compression paddle of General Electric DBT system that was available at the MGH. Given these requirements, two acrylic boxes were built, one on the bottom, serving as the matching liquid container, and one on the top, holding the motion stage assembly in place. Two Big Easy Drivers, powered by a 12 V/5 A power supply, and an Arduino Uno were used to actuate and control the motors. For the bottom box to safely contain the coupling liquid, all of its interior edges were sealed with a silicon-based sealant (General Electric), which was specifically formulated for plastics. Moreover, a lid attached to the top box via hinges was used to constrain ethanol's evaporation. The various parts of the system are shown in **Figure 7**.

6.2. The software

LABVIEW was used as the main programming tool for data acquisition, mechanical motion control, and synchronization between the two. PNA-X (N5242), a programmable network analyzer by Keysight, was used for data acquisition and LABVIEW Interface for Arduino (LIFA) was installed on the workstation (Windows 10) to enable the connection between Aruino and LABVIEW. Using the Stepper Motor Library of LIFA, the motors were configured to have a default speed of 2000 steps/sec in each section of the motion path. The collected data was the two-port s-parameters of the AVAs, which included the phase and magnitude information; and it was recorded on a folder that was shared between the operating system of the PNA-X and the workstation computer. For simplicity, in the first imaging experiments, instead of using triggers to time different events in the acquisition process, a short delay, was utilized after the command was sent to the PNA-X to ascertain that the data collection at each point of the path was complete before moving to the next position. The value of the delay was determined approximately with trial and error. As displayed in **Figure 8**, at any time during the motion on the default path, only one motor is active.

http://dx.doi.org/10.5772/intechopen.69726

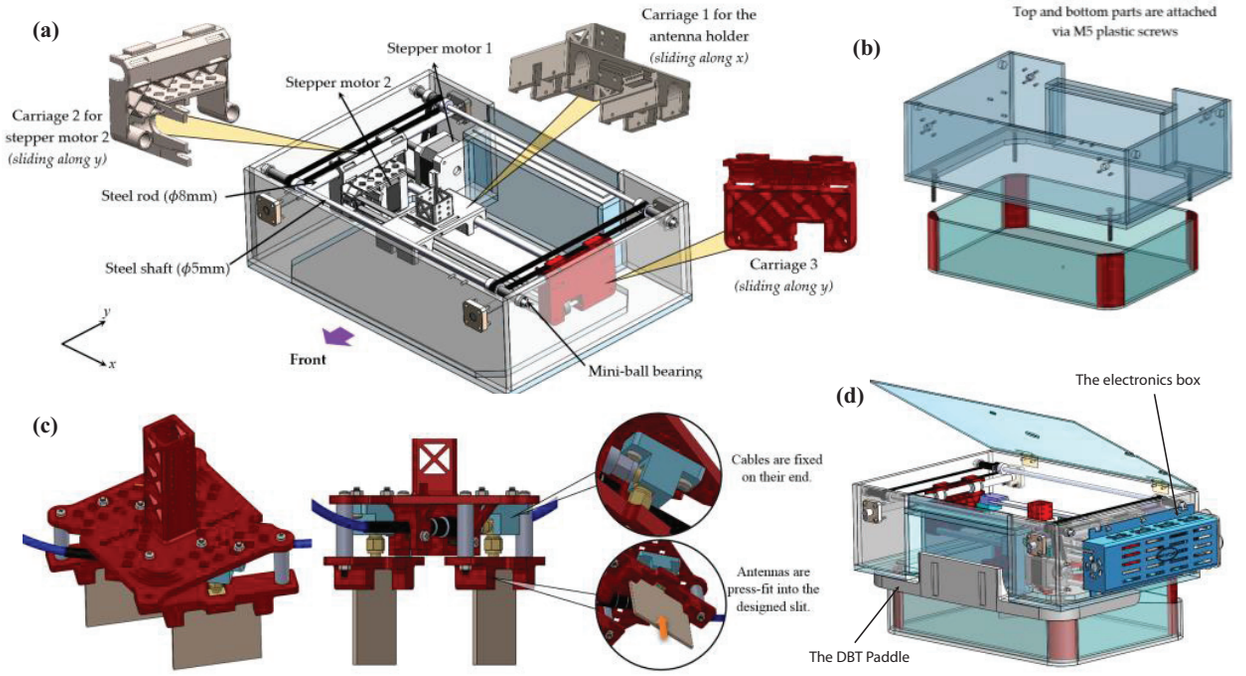

Figure 7. Schematic diagram of the mechanical parts of the motion stage: (a) The gantry on top, responsible for moving the transducer array in two dimensions, (b) the attachment mechanism for the top and bottom boxes, (c) the antenna holder with a structure that assures cables are fixed on the end connected to the antenna, (d) the complete assemblage, including the electronics box, fitted into the DBT paddle.

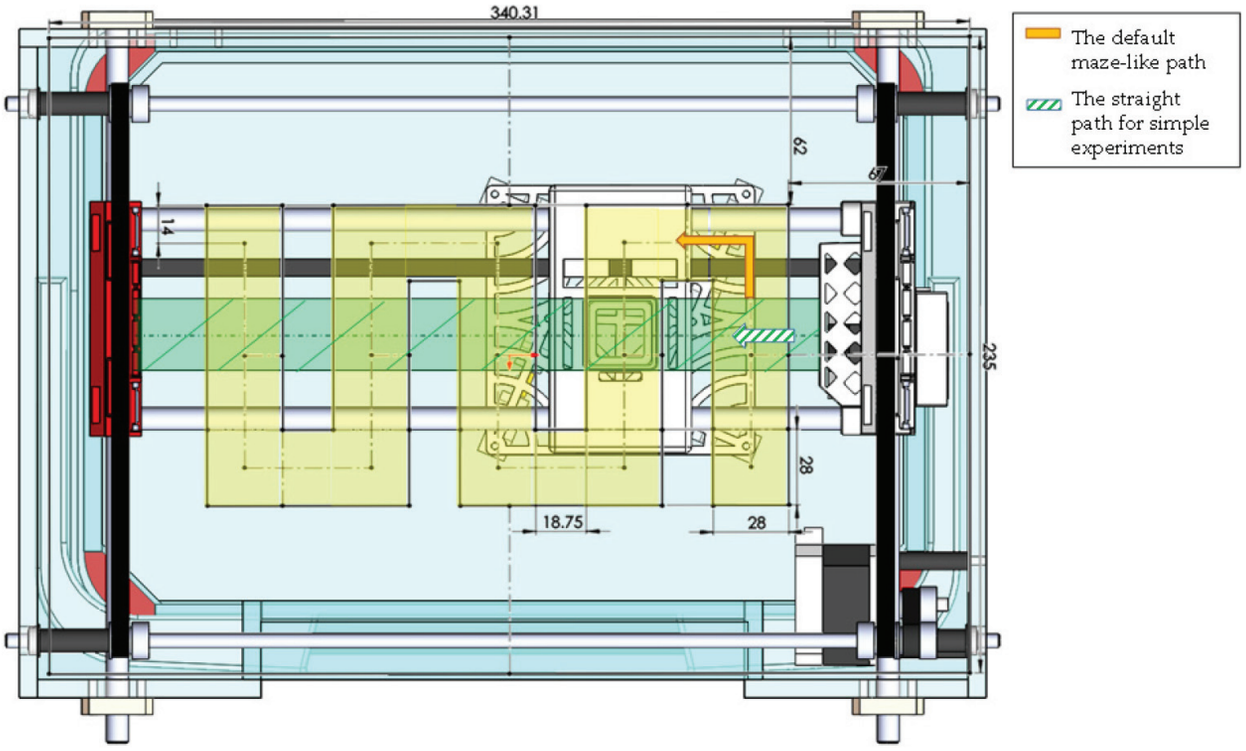

Figure 8. The two-dimensional trajectory viewed from the top. The default path is set to be maze-like (with adjustable number of back-and-forth sections) so that the whole breast volume can be covered. The straight path was used in initial experiments as will be described later.

7. Proof-of-concept experiment and simulation

To show the capabilities of the NRI system as an independent system, a simple measurement was designed to firstly acquire the data from a scattering object inside a known medium, and secondly to retrieve the dialectic map of the medium and the object. This first measurement was simplified using the following requirements: (1) The medium is required to be homogenous with known dielectric properties close to those of breast fat; (2) the object needs to be a strong scatterer of simple and known shape and big size so that it can be easily detected; (3) the data acquisition is to be done in a straight line, instead of the maze-like path, passing through the centroid of the object; (4) the air gap between the NRI system (bottom container) and the under-test medium is to be eliminated. The conditions were realized by using a stainless steel bearing ball of 1-inch diameter inside a container filled with sunflower oil. It is conspicuous that the conditions described differ largely from the reality in which the breast tissue is highly heterogeneous, the contrast between malignant and healthy tissues is comparatively small, and the size of tumors in their early stages is in order of millimeters; however, this first test was intentionally designed to avoid complexities for the purpose of proof-of-concept. Besides this experiment, a simulation was carried out to illustrate how the bimodal imaging using the DBT and the near-field radar system works. The details of this simulation are given in subsection 7.2 and 7.4.

7.1. The bearing ball imaging experiment setup

Required by the imaging algorithm, both the background data, when there was no scatterer in the medium, and the total field data, when the ball was placed in the oil container, had to be acquired. Accordingly, the NRI system was placed on top of the container, partially immersed in the oil, and 25 sets of data at 25 equally spaced positions on the motion path were obtained from the medium with and without the bearing ball inside it. In the case of total field measurements, the ball, seated at the bottom of the container, was positioned at various distances from the centre of the bottom acrylic sheet. The antennas' center motion path was defined to be a straight line passing through the center of the ball, when the system was viewed from the top, as shown with a hashed arrow in **Figure 8**. The layout of the experiment is illustrated in **Figure 9**.

To obtain a more accurate model of the coupling liquid that was used for both the SAR analysis and imaging algorithm, the complex permittivity of absolute ethanol was measured by the PNA-X material measurement software (Keysight Material Measurement Suite 2015), and it was compared against the one reported in the literature [95]. The result is in good agreement with the one reported by Sato et al., as shown in **Figure 10**.

7.2. Imaging algorithm

The total electric field $\boldsymbol{E}(\boldsymbol{r}, \omega)$, assumed to be a function of the vector position $\boldsymbol{r}$ and frequency ω, due to electromagnetic propagation into a three-dimensional medium can be expressed by Helmholtz equation as [111]

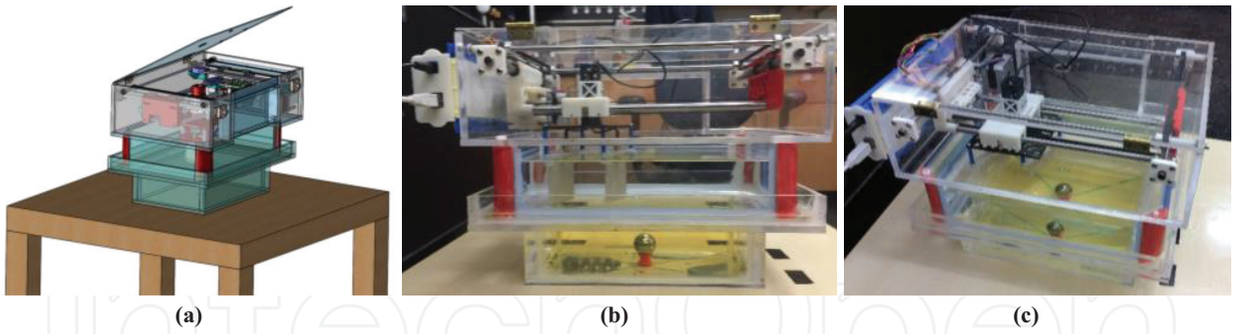

Figure 9. The bearing ball imaging experiment: (a) the entire setup with the NRI system on top of the oil container which is seated on a low-density wooden table. (b) The front and (c) perspective views of the experiment showing how the ethanol container is partially submerged in oil with the aim of air gap elimination. As shown, the ball rests on a plastic base whose diameter is smaller than the ball itself and thus shadowed by the ball when the microwaves illuminate the medium.

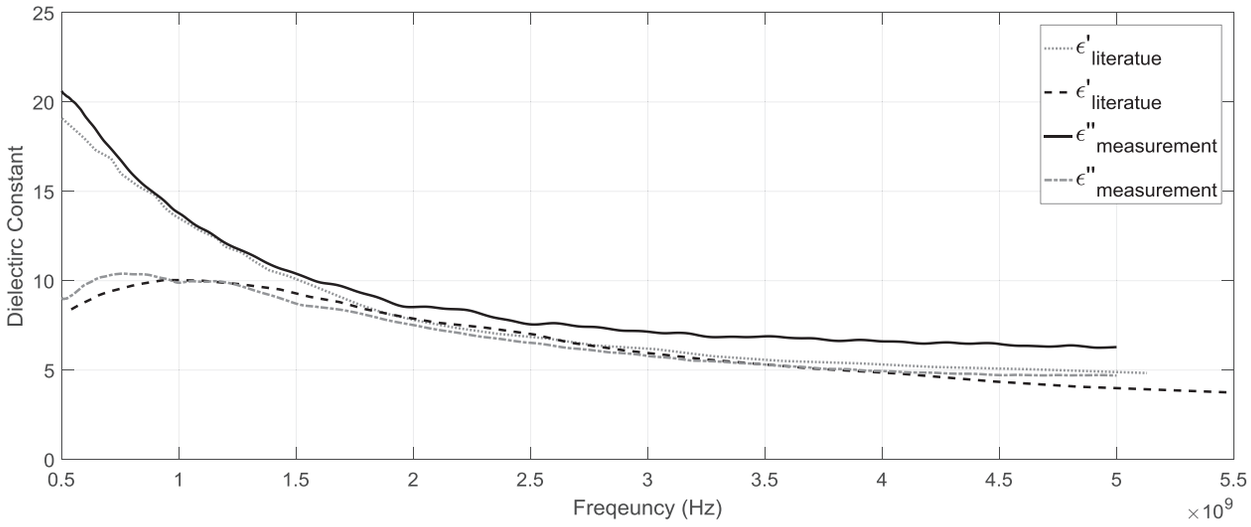

Figure 10. The dielectric relaxation result of ethanol; measurement versus what is reported in the literature [97]. ϵ' and ϵ'' respectively denote the real and imaginary part of complex permittivity.

$$\nabla \times \nabla \boldsymbol{E}(\boldsymbol{r}, \omega) - k^2(\boldsymbol{r}, \omega)\boldsymbol{E}(\boldsymbol{r}, \omega) = j\omega\mu_0 \boldsymbol{I}(\boldsymbol{r}, \omega) \tag{5}$$

where $k(\boldsymbol{r}, \omega) = \sqrt{\varepsilon_0 \varepsilon_r \mu_0(\boldsymbol{r}, \omega)}$ is the wavenumber in the medium with ε_0 being the vacuum permittivity, $\varepsilon_r(\boldsymbol{r}, \omega)$ being the relative complex permittivity, and μ_0 being the vacuum permeability; and $\boldsymbol{I}(\boldsymbol{r}, \omega)$ is the microwave excitation source in the case of near-field radar radiation. The relative complex permittivity of a material is defined as $\varepsilon_r = \varepsilon'_r - j\sigma/\omega\varepsilon_0$, where ε'_r is the real part, and $\varepsilon''_r = \sigma/\omega\varepsilon_0$ is the imaginary part that depends on the conductivity of the material σ. The total electric field $\boldsymbol{E}(\boldsymbol{r}, \omega)$ is composed of the background $\boldsymbol{E_b}(\boldsymbol{r}, \omega)$ and scattered field $\boldsymbol{E_s}(\boldsymbol{r}, \omega)$, or mathematically:

$$\boldsymbol{E}(\boldsymbol{r}, \omega) = \boldsymbol{E}_b(\boldsymbol{r}, \omega) + \boldsymbol{E}_s(\boldsymbol{r}, \omega) \tag{6}$$

The background field is usually modeled with the help of simulations or analytical methods, and the scattered field is obtained by subtracting the background field from the measured total

field. Since $\boldsymbol{E_b}(r, \omega)$ also satisfies the Helmholtz equation, with $k_b(\boldsymbol{r}, \omega)$ instead of $k(\boldsymbol{r}, \omega)$ and the solution

$$\boldsymbol{E}_b(\boldsymbol{r}, \omega) = j\omega \int \boldsymbol{G_b}(\boldsymbol{r}, \boldsymbol{r}', \omega) I(\boldsymbol{r}', \omega) d\boldsymbol{r}' \tag{7}$$

where $G_b(r\,, r', \omega)$ is dyadic Green's function and a solution of

$$\nabla \times \nabla \boldsymbol{G}_b(\boldsymbol{r}, \omega) - k_b^2(\boldsymbol{r}, \omega) \boldsymbol{G}_b(\boldsymbol{r}, \omega) = \tilde{\boldsymbol{I}} \delta(\boldsymbol{r} - \boldsymbol{r}') \tag{8}$$

with $\tilde{\boldsymbol{I}}$ being the unit dyad, the scattered field $\boldsymbol{E}_s(\boldsymbol{r}, \omega)$ can be solved as

$$\boldsymbol{E}_s(\boldsymbol{r}, \omega) = \int \boldsymbol{G_b}(\boldsymbol{r}, \boldsymbol{r}', \omega) k_b^2(\boldsymbol{r}', \omega) \boldsymbol{E}(\boldsymbol{r}, \omega) \chi(\boldsymbol{r}', \omega) dr' \tag{9}$$

in which is $\chi = (\varepsilon_r(\boldsymbol{r}, \omega) - \varepsilon_{r,b}(\boldsymbol{r}, \omega))/\varepsilon_{r,b}(\boldsymbol{r}, \omega)$, the contrast parameter, and $\varepsilon_{r,b}(\boldsymbol{r}, \omega)$ is the relative permittivity of the background medium. In cases where the contrast parameter is comparatively small, BORN approximation can be applied by replacing the total field with the background field in Eq. (9), which results in

$$\boldsymbol{E}_s(\boldsymbol{r}, \omega) \approx \int \boldsymbol{G_b}(\boldsymbol{r}, \boldsymbol{r}', \omega) k_b^2(\boldsymbol{r}', \omega) \boldsymbol{E}_b(\boldsymbol{r}, \omega) \chi(\boldsymbol{r}', \omega) dr' \tag{10}$$

that can be solved now. Making use of the FDFD method and discretization, Eq. (10) can be linearized in terms of the unknown–the contrast parameter– as follows [112]:

$$\mathbf{y} = \boldsymbol{A}\chi + \mathbf{e} \tag{11}$$

where $\mathbf{y} \in \mathbb{C}^M$ is the measurement vector obtained by the receiving antenna, $\boldsymbol{A} \in \mathbb{C}^{M \times N}$ is the sensing matrix, $\boldsymbol{\chi} \in \mathbb{C}^N$ is the unknown contrast vector, and $\mathbf{e} \in \mathbb{C}^M$ is the modeled noise. The sensing matrix $\boldsymbol{A}$ is generated by the Green's functions of the background medium. Note that for the DBT-NRI system, the background Green's functions are computed using a full wave model (like HFSS ANSYS) in which the dielectric properties of a healthy heterogeneous breast is derived from the fat content of the DBT image. For the results of the bearing ball experiment, presented in this chapter, the background Green's functions are computed from modeling the mechatronic system without the metallic scatterer (ball), also using HFSS ANSYS. As the number of measurements, M, is much less than the number of unknowns N, a regularization method is to be used to reduce the ill-posedness of the solution. In this case, Tikhonov regularization scheme can be applied, which seeks the solution to the succeeding optimization problem [112]:

$$\min \left|\left|\boldsymbol{A}\boldsymbol{\chi} - \mathbf{y}\right|\right|_{\ell_2}^2 + \gamma \left|\left|\boldsymbol{\chi}\right|\right|_{\ell_p}^p \tag{12}$$

$$\text{Subject to} \begin{cases} \mathbf{Re}\left(\text{diag}(\varepsilon_b)\mathbf{x} + \varepsilon_b\right) \geq 1 \\ \mathbf{Im}\left(\text{diag}(\varepsilon_b)\mathbf{x} + \varepsilon_b\right) \geq 0 \end{cases} \tag{13}$$

in which ℓ_p denotes norm-p and γ is the regularization parameter. When this problem is solved using p = 2, indicating that the ℓ_2 is used as a regularizer function, a simple closed-form solution is given by the following equation:

$$\chi = (\boldsymbol{A}^H \boldsymbol{A} + \gamma \boldsymbol{I})^{-1} \boldsymbol{A}^H \mathbf{y} \tag{14}$$

where $\boldsymbol{A}^H$ is the Hermitian of matrix **A** and γ is is selected by trial and error with the aim of achieving an efficient and smooth solution. Other convex optimization approaches can also be used. Specifically, when the problem is solved using p = 1, indicating the use of the ℓ_1 as a regularizer function, sparsity can be imposed to the solution—see for example [111]. This regularizer function is of special interest when the DBT and the NRI are operating together.

7.3. Results

7.3.1. Images reconstructed from computational simulations

To demonstrate the efficacy of the hybrid bimodal DBT/NRI system, the fat percentage of the DBT image of a breast was used to model the electromagnetic scattering of a breast with and without a cancer lesion. **Figure 11(a)** shows the ground truth model. A total of six antennas at three different frequencies, 500, 600, and 700 MHz, were used on the periphery of the breast model, inside a bolus liquid, that enhanced the electromagnetic coupling into the tissue [110]. The method described in [106], which used the ℓ_1 norm as a regularizer function, was employed to estimate the real and imaginary parts of the contrast variable χ. As shown in **Figure 11(b)**, the contrast source variable successfully localized the tumor, albeit of being surrounded by fibroglandular tissue.

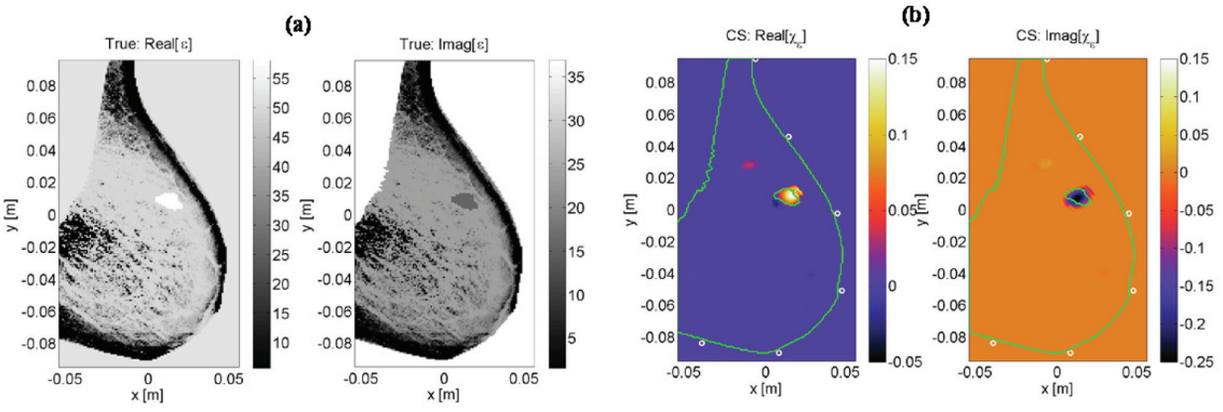

Figure 11. (a) The ground truth complex permittivity, the real (left) and the imaginary (right) part. (b) Successfully reconstructed contrast source variable χ, as defined in Eq. (9), after using the imaging technique described in [106]; (left) real and (right) imaginary parts.

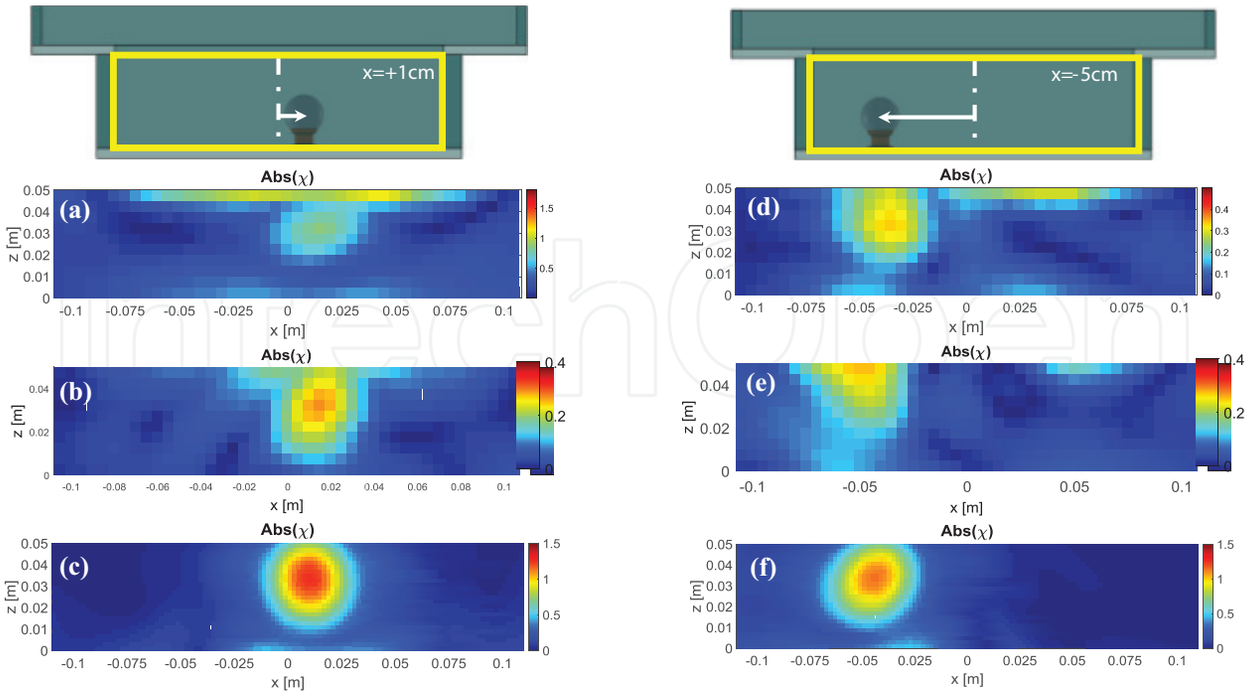

Figure 12. Reconstructed images of a bearing ball embedded in sunflower oil. Images obtained from the data acquired by a regular SMA cable (a), a phase-stable cable (b), and simulation (c), respectively, when the ball was located 1 cm off center. Parts (d)–(f) show similar images for when the ball was 5 cm off center.

7.3.2. Images reconstructed from the experiment

Implementing the imaging algorithm described in the previous subsection, the images of the oil-bearing ball medium were reconstructed for different cases when the ℓ_2 norm is used as the regularizer. As shown in **Figure 12**, the measurements were carried out for various ball locations (two of which are shown here) and for two type of cables, regular SMA cable and phase-stable cable. Despite the presence of some artifacts, the normalized dielectric maps from the measurements agree well with those obtained from the simulations. In overall, though phase-stable cables improved the phase response of the system significantly, they were not as effective in the final imaging results. These images demonstrate that the NRI system is capable of collecting meaningful data and generating images for a simply configured medium.

8. Conclusions

In this chapter, the basics of a bimodal imaging system aimed at early detection of breast cancer were reviewed and some preliminary computational and experimental results were presented. It was noted that the conventional mammography has raised some concerns due to the reported rates of false-positive and false-negative results, as well as overdiagnosis. Digital breast tomosynthesis has been able to compensate for some of these problems, only up to a certain degree, by enabling multi-layer imaging of the breast; and it has resulted in improved specificity and sensitivity. However, the low contrast between malignant and fibroglandular tissues in the X-ray frequencies still remains as a drawback of X-ray-based

breast screening. Near-field radar imaging (NRI), as a cheap and safe modality, has the potential to alleviate the problem of low contrast inasmuch as the aforementioned tissues show more contrast at microwave frequencies. Founded on this observation, an NRI mechatronic system, compatible with the DBT, was developed to be used as an auxiliary diagnosis tool, in a co-registered manner. The performance of the NRI component of this system was experimentally evaluated in a near-ideal case, and the achieved results showed its capability in imaging a strong scatterer in a homogenous medium. Computational results were also carried out, showing the efficacy of the bimodal system to detect tumors surrounded by fibroglandular tissue. It was also shown, through specific absorption rate analysis, that the radiation of the implemented antennas is safe for humans, according to the standards. Our next step in this exciting work is to pilot the hybrid DBT/NRI system using more realistic phantoms, as well as human patients.

Author details

Ashkan Ghanbarzadeh Dagheyan[2], Ali Molaei[1], Richard Obermeier[1], Aida K. Martinez[3] and Jose Martinez Lorenzo[1,2]*

*Address all correspondence to: j.martinez-lorenzo@neu.edu

1 Department of Mechanical Engineering, Northeastern University, Boston, MA, USA

2 Department of Electrical Engineering, Northeastern University, Boston, MA, USA

3 Harvard Vanguard Medical Associates, Wellesley, MA, USA

References

[1] Surveillance, Epidemiology, and End Results (SEER) Program (www.seer.cancer.gov) Research Data (1973–2013), National Cancer Institute, DCCPS, Surveillance Research Program, Surveillance Systems Branch, released April 2016, based on the November 2015 submission

[2] National Program of Cancer Registries (NPCR), Center for Disease Control and Prevention (CDC), Available: https://nccd.cdc.gov/uscs/toptencancers.aspx, (Accessed: 13 May 2016)

[3] Howlader N, Noone AM, Krapcho M, Garshell J, Neyman N, Altekruse SF, Kosary CL, Yu M, Ruhl J, Tatalovich Z, Cho H, Mariotto A, Lewis DR, Chen HS, Feuer EJ, Cronin KA (eds). SEER Cancer Statistics Review. 1975–2010. Bethesda, MD: National Cancer Institute, http://seer.cancer.gov/csr/1975_2010/, based on November 2012 SEER data submission, posted to the SEER web site, April 2013

[4] Sugimura T. et al. Heterocyclic amines: Mutagens/carcinogens produced during cooking of meat and fish. Cancer Science. 2004;**95**(4). :290–299

[5] Puangsombat K, et al. Occurrence of heterocyclic amines in cooked meat products. Meat science. 2012;**90**(3):739–746

[6] Beasley JM, et al. Associations of serum insulin-like growth factor-I and insulin-like growth factor-binding protein 3 levels with biomarker-calibrated protein, dairy product and milk intake in the Women's Health Initiative. British Journal of Nutrition. 2014;**111** (05): 847–853

[7] Casa AJ, et al. Estrogen and insulin-like growth factor-I (IGF-I) independently down-regulate critical repressors of breast cancer growth. Breast Cancer Research and Treatment. 2012;**132**(1):61–73

[8] Torfadottir JE, et al. Milk intake in early life and risk of advanced prostate cancer. American Journal of Epidemiology. 2011;**175**(2):144-153

[9] Tate PL, Bibb R, Larcom LL. Milk stimulates growth of prostate cancer cells in culture. Nutrition and Cancer. 2011;**63**(8):1361–1366

[10] Buehring GC, et al. Exposure to bovine leukemia virus is associated with breast cancer: A case-control study. PloS one. 2015;**10**(9):e0134304

[11] Giovanna, Mesa, et al. Bovine leukemia virus gene segment detected in human breast tissue. Open Journal of Medical Microbiology, 2013;**3**(1):84-90

[12] Torre, Lindsey A., et al. Global cancer statistics, 2012. CA: a cancer journal for clinicians. 2015;**65**(2):87-108

[13] Grant WB. Trends in diet and Alzheimer's disease during the nutrition transition in Japan and developing countries. Journal of Alzheimer's Disease. 2014;**38**(3):611–620

[14] Key TJ, et al. The effect of diet on risk of cancer. The Lancet. 2002;**360**(9336):861–868

[15] McPherson K, Steel CM, and Dixon JM. Breast cancer-epidemiology, risk factors, and genetics. BMJ: British Medical Journal. 2000;**321**(7261):624

[16] Mensah GA. Ischaemic heart disease in Africa. Heart. 2008;**94**(7):836–843

[17] Shaper AG, Jones KW. Serum-cholesterol, diet, and coronary heart-disease in Africans and Asians in Uganda. International Journal of Epidemiology. 2012;**41**(5):1221–1225

[18] Sepehrnia B. et al. Genetic studies of human apolipoproteins. X. The effect of the apolipoprotein E polymorphism on quantitative levels of lipoproteins in Nigerian blacks. American Journal of Human Genetics. 1989;**45**(4):586

[19] American Cancer Society. Breast Cancer Facts & Figures 2013–2014. Atlanta: American Cancer Society. Inc. 2013

[20] Christiansen CL, et al. Predicting the cumulative risk of false-positive mammograms. Journal of the National Cancer Institute. 2000;**92**(20):1657–1666

[21] Castells X, Eduard M, Francesc M. Cumulative false positive recall rate and association with participant related factors in a population based breast cancer screening programme. Journal of Epidemiology and Community Health. 2006;**60**(4):316–321

[22] Hubbard, RA, et al. Cumulative probability of false-positive recall or biopsy recommendation after 10 years of screening mammography: A cohort study. Annals of Internal Medicine. 2011;**155**(8):481–492

[23] Cheng HD, et al. Automated breast cancer detection and classification using ultrasound images: A survey. Pattern Recognition. 2010;**43**(1):299–317

[24] Carril JM. et al. Contribution of 99mTc-MIBI scintimammography to the diagnosis of non-palpable breast lesions in relation to mammographic probability of malignancy. Anticancer Research. 1996;**17**(3B):1677–1681

[25] Gram IT, Lund E, Slenker SE. Quality of life following a false positive mammogram. British Journal of Cancer. 1990;**62**(6):1018

[26] Brewer NT, Salz T, Lillie SE. Systematic review: The long-term effects of false-positive mammograms. Annals of Internal Medicine. 2007;**146**(7):502–510

[27] Witek-Janusek L, Gabram S, Mathews HL. Psychologic stress, reduced NK cell activity, and cytokine dysregulation in women experiencing diagnostic breast biopsy. Psychoneuroendocrinology. 2007;**32**(1):22–35

[28] Brodersen J, Siersma VD. Long-term psychosocial consequences of false-positive screening mammography. The Annals of Family Medicine. 2013;**11**(2):106–115

[29] Kerlikowske K, et al. Effect of age, breast density, and family history on the sensitivity of first screening mammography. Jama. 1996;**276**(1):33–38

[30] Dabbous, FM, et al. Comparison of false-negative probabilities for digital and film mammography within a large health care organization. ASCO Annual Meeting Proceedings. 2014;**32**(15_suppl)

[31] Tilanus-Linthorst M, et al. A BRCA1/2 mutation, high breast density and prominent pushing margins of a tumor independently contribute to a frequent false-negative mammography. International Journal of Cancer. 2002;**102**(1):91–95

[32] Meeson, S., et al. Image features of true positive and false negative cancers in screening mammograms. The British journal of radiology. 2003;**76**(901):13-21

[33] Zackrisson S, et al. Rate of over-diagnosis of breast cancer 15 years after end of Malmö mammographic screening trial: Follow-up study. The BMJ. 2006;**332**(7543):689–692

[34] Zahl P-H, Strand BH, Mæhlen J. Incidence of breast cancer in Norway and Sweden during introduction of nationwide screening: prospective cohort study. The BMJ. 2004;**328**(7445): 921–924

[35] Paci E. et al. Overdiagnosis in screening: Is the increase in breast cancer incidence rates a cause for concern Journal of Medical Screening. 2004;**11**(1):23–27

[36] Jonsson H, Johansson R, Lenner P. Increased incidence of invasive breast cancer after the introduction of service screening with mammography in Sweden. International Journal of Cancer. 2005;**117**(5):842–847

[37] Beckmann, Kerri, et al. Estimates of over-diagnosis of breast cancer due to population-based mammography screening in South Australia after adjustment for lead time effects. Journal of medical screening. 2015;**22**(3)127-135

[38] Puliti D, et al. Overdiagnosis in mammographic screening for breast cancer in Europe: A literature review. Journal of Medical Screening. 2012;**19(**1_suppl):42–56

[39] Cole EB, et al. Diagnostic accuracy of digital mammography in patients with dense breasts who underwent problem-solving mammography: Effects of image processing and lesion type 1. Radiology. 2003;**226**(1):153–160

[40] Baldwin P. Digital breast tomosynthesis. Radiologic Technology. 2009;**81**(1):57-74M

[41] Pisano ED, et al. Diagnostic performance of digital versus film mammography for breast-cancer screening. New England Journal of Medicine. 2005;**353**(17):1773–1783

[42] Park JM, et al. Breast tomosynthesis: Present considerations and future applications 1. Radiographics. 2007;**27**(suppl_1):S231-S240

[43] Teertstra HJ, et al. Breast tomosynthesis in clinical practice: initial results. European Radiology. 2010;**20**(1):16–24

[44] Bernardi, D., et al. Application of breast tomosynthesis in screening: incremental effect on mammography acquisition and reading time. The British journal of radiology. 2012;**85**(1020): e1174-e1178

[45] Gur D, et al. Digital breast tomosynthesis: Observer performance study. American Journal of Roentgenology. 2009;**193**(2):586–591

[46] Houssami N, et al. Breast screening using 2D-mammography or integrating digital breast tomosynthesis (3D-mammography) for single-reading or double-reading–Evidence to guide future screening strategies. European Journal of Cancer. 2014;**50**(10): 1799–1807

[47] Bernardi D, et al. Effect of integrating 3D-mammography (digital breast tomosynthesis) with 2D-mammography on radiologists' true-positive and false-positive detection in a population breast screening trial. European Journal of Cancer. 2014;**50**(7):1232–1238

[48] Svahn TM, Macaskill P, Houssami N. Radiologists' interpretive efficiency and variability in true-and false-positive detection when screen-reading with tomosynthesis (3D-mammography) relative to standard mammography in population screening. The Breast. 2015;**24**(6):687–693

[49] Gilbert, Fiona J., et al. Accuracy of digital breast tomosynthesis for depicting breast cancer subgroups in a UK retrospective reading study (TOMMY trial). Radiology. 2015;**22**(3):697-706

[50] Houssami N, et al. Digital breast tomosynthesis (3D-mammography) screening: A pictorial review of screen-detected cancers and false recalls attributed to tomosynthesis in prospective screening trials. The Breast. 2016;**26**:119–134

[51] Rappaport C, Tivnan M, Kaeli E, Obermeier R, Moore R, Kopans D, Martinez Lorenzo J. Fusing microwave radar imaging with digital breast tomosynthesis for high contrast, high resolution breast cancer detection. Radiological Society of North America. 2014 Scientific Assembly and Annual Meeting, Chicago IL. Available: http://archive.rsna.org/2014/14018670.html [Accessed 17-February-2015]

[52] Meaney PM, et al. A clinical prototype for active microwave imaging of the breast. Microwave Theory and Techniques, IEEE Transactions on. 2000;**48**(11):1841–1853

[53] Lazebnik M, et al. A large-scale study of the ultrawideband microwave dielectric properties of normal, benign and malignant breast tissues obtained from cancer surgeries. Physics in Medicine and Biology. 2007;**52**(20):6093

[54] Halter RJ, et al. The correlation of in vivo and ex vivo tissue dielectric properties to validate electromagnetic breast imaging: initial clinical experience. Physiological Measurement. 2009;**30**(6):S121

[55] Golnabi AH. Computational aspect of tomographic microwave imaging for biomedical applications. DARTMOUTH COLLEGE. ProQuest Dissertations Publishing. 2012. 3544495

[56] Meaney PM, Paulsen KD, Ryan TP. Two-dimensional hybrid element image reconstruction for TM illumination. Antennas and Propagation, IEEE Transactions. 1995;**43**(3):239–247

[57] Li D, Meaney PM, Paulsen KD. Conformal microwave imaging for breast cancer detection. Microwave Theory and Techniques. IEEE Transactions. 2003;**51**(4):1179–1186

[58] David W. et al. Three-dimensional microwave breast imaging: Dispersive dielectric properties estimation using patient-specific basis functions. Medical Imaging, IEEE Transactions. 2009;**28**(7):969–981

[59] Joachimowicz N, Pichot C, Hugonin J-P. Inverse scattering: An iterative numerical method for electromagnetic imaging. Antennas and Propagation, IEEE Transactions. 1991;**39**(12):1742–1753

[60] Franchois A, Pichot C. Microwave imaging-complex permittivity reconstruction with a Levenberg-Marquardt method. Antennas and Propagation. IEEE Transactions. 1997;**45**(2):203–215

[61] Rubk T, et al. Nonlinear microwave imaging for breast-cancer screening using Gauss–Newton's method and the CGLS inversion algorithm. Antennas and Propagation. IEEE Transactions. 2007;**55**(8):2320–2331

[62] Gilmore C, et al. Microwave biomedical data inversion using the finite-difference contrast source inversion method. Antennas and Propagation. IEEE Transactions. 2009;**57**(5):1528–1538

[63] Dong Q, Rappaport CM. Microwave subsurface imaging using direct finite-difference frequency-domain-based inversion. Geoscience and Remote Sensing. IEEE Transactions. 2009;**47**(11):3664–3670

[64] Firoozabadi R, Miller EL. Finite element modeling of electromagnetic scattering for microwave breast cancer detection. Skin. 2010;**15**(40.1):0–74

[65] Meaney PM, et al. Initial clinical experience with microwave breast imaging in women with normal mammography. Academic Radiology. 2007;**14**(2):207–218

[66] Neira LM, Van Veen BD, Hagness SC. Investigation of high-resolution microwave breast imaging using a 3-D inverse scattering algorithm with a variable-strength spatial prior constraint. Radio Science Meeting (Joint with AP-S Symposium). 2015;USNC-URSI. IEEE. 2015

[67] Sun YP, et al. CS based confocal microwave imaging algorithm for breast cancer detection. Technology and Health Care Preprint. 2016:1–9

[68] Baran A, et al. Breast cancer imaging using microwave tomography with radar-derived prior information. Radio Science Meeting (Joint with AP-S Symposium), 2014 USNC-URSI. IEEE. 2014

[69] Golnabi AH, Meaney PM, Paulsen KD. Tomographic microwave imaging with incorporated prior spatial information. Microwave Theory and Techniques. IEEE Transactions. 2013;**61**(5):2129–2136

[70] Golnabi AH, Meaney PM, Paulsen KD. 3D microwave tomography of the breast using prior anatomical information. Medical physics. 2016;**43**(4):1933–1944

[71] Klemm M, et al. Radar-based breast cancer detection using a hemispherical antenna array—experimental results. Antennas and Propagation, IEEE Transactions. 2009;**57**(6):1692–1704

[72] Klemm M, et al. Microwave radar-based breast cancer detection: Imaging in inhomogeneous breast phantoms. Antennas and Wireless Propagation Letters. IEEE. 2009;**8**:1349–1352

[73] Klemm M, et al. Experimental and clinical results of breast cancer detection using UWB microwave radar. Antennas and Propagation Society International Symposium; 2008. AP-S 2008. IEEE. IEEE, 2008

[74] Lai JCY, et al. UWB microwave imaging for breast cancer detection—Experiments with heterogeneous breast phantoms. Progress in Electromagnetics Research M. 2011;**16**:19–29

[75] Lazaro A, Girbau D, Villarino R. Simulated and experimental investigation of microwave imaging using UWB. Progress in Electromagnetics Research. 2009;**94**:263–280

[76] Yu C, et al. Active microwave imaging II: 3-D system prototype and image reconstruction from experimental data. Microwave Theory and Techniques. IEEE Transactions. 2008;**56**(4):991–1000

[77] Henriksson T, et al. Quantitative microwave imaging for breast cancer detection using a planar 2.45 GHz system. Instrumentation and Measurement. IEEE Transactions on. 2010;**59**(10):2691–2699

[78] Franchois A, et al. Quantitative microwave imaging with a 2.45 GHz planar microwave camera. Medical Imaging, IEEE Transactions. 1998;**17**(4):550–561

[79] Bassi M, et al. An integrated microwave imaging radar with planar antennas for breast cancer detection. Microwave Theory and Techniques, IEEE Transactions. 2013;**61**(5):2108–2118

[80] Bond EJ, et al. Microwave imaging via space-time beamforming for early detection of breast cancer. Antennas and Propagation, IEEE Transactions. 2003;**51**(8):1690–1705

[81] Li X, et al. Microwave imaging via space-time beamforming: Experimental investigation of tumor detection in multilayer breast phantoms. Microwave Theory and Techniques, IEEE Transactions. 2004;**52**(8):1856–1865

[82] Eleuterio R, Medina A, Conceicao RC. Initial study with microwave imaging of the axilla to aid breast cancer diagnosis. Radio Science Meeting (Joint with AP-S Symposium). 2014 USNC-URSI. IEEE

[83] Grzegorczyk TM, Meaney PM, Paulsen KD. Microwave tomographic imaging for breast cancer chemotherapy monitoring. Antennas and Propagation (EuCAP), 2014 8th European Conference. IEEE; 2014

[84] Fu L, et al. Microwave radar imaging using a solid state spintronic microwave sensor. Applied Physics Letters. 2014;**105**(12):122406

[85] Bucci OM, et al. Characterization of a laboratory setup for assessing the feasibility of magnetic nanoparticles enhanced microwave imaging. Submitted to EuCAP. 2016

[86] Golnabi AH. Computational Aspect of Tomographic Microwave Imaging for Biomedical Applications. Order No. 3544495 Dartmouth College, 2012. Ann Arbor: ProQuest. Web. 13 Nov. 2016

[87] Fang Q, et al. Combined optical imaging and mammography of the healthy breast: Optical contrast derived from breast structure and compression. Medical Imaging, IEEE Transactions on. 2009;**28**(1):30–42

[88] Jiang H, et al. Ultrasound-guided microwave imaging of breast cancer: Tissue phantom and pilot clinical experiments. Medical Physics. 2005;**32**(8):2528–2535

[89] Fei P, et al. A miniaturized antipodal Vivaldi antenna with improved radiation characteristics. Antennas and Wireless Propagation Letters. IEEE. 2011;**10**:127–130

[90] Bourqui J, Okoniewski M, Fear EC. Balanced antipodal Vivaldi antenna for breast cancer detection. Antennas and Propagation, 2007. EuCAP 2007. The Second European Conference on. IET, 2007

[91] Molaei A, et al. Miniaturized UWB Antipodal Vivaldi Antenna for a mechatronic breast cancer imaging system. Antennas and Propagation & USNC/URSI National Radio Science Meeting, 2015 IEEE International Symposium on. IEEE. 2015

[92] Buchner R, Hefter GT, May PM. Dielectric relaxation of aqueous NaCl solutions. The Journal of Physical Chemistry A. 1999;**103**(1):1–9

[93] Sato T, Buchner R. Dielectric relaxation processes in ethanol/water mixtures. The Journal of Physical Chemistry A. 2004;**108**(23):5007–5015

[94] Lu Z, et al. Dielectric relaxation in dimethyl sulfoxide/water mixtures studied by microwave dielectric relaxation spectroscopy. The Journal of Physical Chemistry A. 2009;**113**(44):12207–12214

[95] Markarian SA, Gabrielyan LS. Dielectric relaxation study of diethyl sulfoxide/water mixtures. Physics and Chemistry of Liquids. 2009;**47**(3):311–321

[96] Kavala AK. Dielectric relaxation behaviour of glycine in aqueous solution medium in the microwave frequency region. Indian Journal of Engineering and Materials Science. 2008;**15**:196–198

[97] Shinyashiki N, et al. Shape of dielectric relaxation curves of ethylene glycol oligomer–water mixtures. The Journal of Chemical Physics. 1998;**109**(22):9843–9847

[98] Kaatze U. Microwave dielectric properties of liquids. Radiation Physics and Chemistry. 1995;**45**(4):549–566

[99] Barthel J, et al. Dielectric spectra of some common solvents in the microwave region. Water and lower alcohols. Chemical Physics Letters. 1990;**165**(4):369–373

[100] Saar D, et al. Ultrasonic and microwave dielectric relaxation of liquid dialkyl carbonates. The Journal of Physical Chemistry. 1978;**82**(23):2531–2535

[101] Undre PB, et al. Dielectric relaxation in ethylene glycol-dimethyl sulfoxide mixtures as a function of composition and temperature. Journal of the Korean Chemical Society. 2012;**56**(4):416–423

[102] Bindu GN, et al. Dielectric studies of corn syrup for applications in microwave breast imaging. Progress In Electromagnetics Research. 2006;**59**:175–186

[103] Garrett JD, Fear EC. Average dielectric property analysis of complex breast tissue with microwave transmission measurements. Sensors. 2015;**15**(1):1199–1216

[104] Dagheyan AG, et al. Characterization of two antipodal Vivaldi antennas for breast cancer near-field radar imaging. Antennas and Propagation (APSURSI), 2016 IEEE International Symposium on. IEEE. 2016

[105] Evaluating Compliance with FCC Guidelines for Human Exposure to Radiofrequency Electromagnetic Fields. OET Bulletin 65, Edition 97-01, August 1997. Accessed at: https://transition.fcc.gov/Bureaus/Engineering_Technology/Documents/bulletins/oet65/oet65.pdf, 13 April, 2016

[106] Martinez-Lorenzo JA, Basukoski A, Quivira F, Rappaport C, Moore R, Kopans D. Composite models for microwave dielectric constant characterization of breast tissues. CD Proceedings. AP-S 2013—IEEE AP-S International Symposium, Orlando, FL, Jul. 2013

[107] The Council Of The European Union, Implementation report on the Council Recommendation limiting the public exposure to electromagnetic fields (0 Hz to 300 GHz), Accessed at http://ec.europa.eu/health/ph_determinants/environment/EMF/implement_rep_en.pdf, 14 April, 2016

[108] IEEE Recommended Practice for Determining the Peak Spatial-Average Specific Absorption Rate (SAR) in the Human Head from Wireless Communications Devices: Measurement Techniques - Redline. IEEE Xplore. IEEE International Committee on Electromagnetic Safety, 22 Jan. 2014. Accessed at http://ieeexplore.ieee.org/stamp/stamp.jsp?tp=&arnumber=6719585, 14 April, 2016

[109] Tan Desmond. Modeling the Specific Absorption Rate Distribution of a Smartphone. 2012 ANSYS Inc. Accessed at: http://resource.ansys.com/staticassets/ANSYS/staticassets/resourcelibrary/techbrief/ab-modeling-specific-absorption-rate-smartphone.pdf, 14 April, 2016

[110] Obermeier R, et al. Imaging breast cancer in a hybrid DBT/NRI system using compressive sensing. Antennas and Propagation & USNC/URSI National Radio Science Meeting; 2015 IEEE International Symposium on. IEEE, 2015

[111] Obermeier R, Martinez-Lorenzo JA. A compressive sensing approach for enhancing breast cancer detection using a hybrid DBT/NRI configuration. Journal of Electromagnetic Waves and Applications. Nov. 2016, doi: 10.1080/09205071.2016.1260064.

[112] Dagheyan AG, et al. Preliminary imaging results and SAR analysis of a microwave imaging system for early breast cancer detection. Engineering in Medicine and Biology Society (EMBC). 2016 IEEE 38th Annual International Conference of the. IEEE; 2016

IntechOpen